Available on CMS information server

CMS AN-2008/080

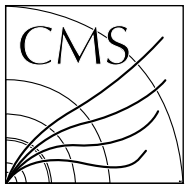

The Compact Muon Solenoid Experiment

Analysis Note

The content of this note is intended for CMS internal use and distribution only

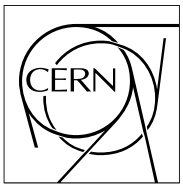

22 September 2008 (v2, 24 September 2008)

QCD studies in CMS with High Transverse Momentum Jets at $\sqrt{s} = 10\,\mathrm{TeV}$.

R. Harris, K. Kousouris, D. Mason
Fermi National Accelerator Laboratory, Batavia, IL, USA

M. Heinrich, A. Oehler, K. Rabbertz
Karlsruhe Institute of Technology, Karlsruhe, Germany

L. Apanasevich, C. Dragoiu, A. Smoron, N. Varelas
University of Illinois at Chicago, Chicago, IL, USA

P. Schieferdecker
CERN, Geneva, Switzerland

Abstract

We present a description of the QCD high p_T jet studies that are planned for CMS at the startup of LHC. The analyses target the first $10\,\mathrm{pb}^{-1}$ of proton-proton collisions at $\sqrt{s} = 10\,\mathrm{TeV}$. The measurements of the inclusive jet and dijet mass cross sections, as well as the measurement of the dijet angular distributions and angular decorrelation are described in detail. The major sources of systematic uncertainties for each analysis are discussed and estimated. All analyses are performed using the CMS Monte Carlo simulated data produced for the CMS Combined Software and Analysis challenge 2008 (CSA08).

Contents

1 Introduction

At the startup of LHC, proton-proton collisions at $\sqrt{s} = 10\,\text{TeV}$ will take place and the CMS detector is expected to accumulate $\mathcal{O}(10\,\text{pb}^{-1})$ of data at this energy. Given the boost of the center-of-mass energy of the colliding protons, the TeV scale will be prompted immediately. With only about $1\,\text{pb}^{-1}$ of integrated luminosity, the transverse momentum will reach beyond any previous collider experiment and the new energy scale can be explored.

The CMS QCD group has developed a detailed plan for studies to be performed at startup, targeting four key measurements which are described in this note:

1. inclusive jet cross section as a function of jet p_T,
2. dijet invariant mass cross section,
3. dijet angular distributions,
4. dijet angular decorrelation.

The note focuses on the feasibility of these measurements with an integrated luminosity of $10\,\text{pb}^{-1}$ and the respective statistical and systematic uncertainties.

1.1 Motivation

In proton-proton collisions, interactions take place between the partons of the colliding protons. Due to the high center-of-mass energy available, the partonic interactions can be in good approximation considered as 2-2 scattering processes. Most of the time, the partonic interactions are soft, leading to small momentum transfer. In those rare cases where the scattering is hard (large momentum transfer), the scattered partons will hadronize into highly collimated bunches of particles that will be measured in the calorimeter as high transverse momentum jets.

The study of the high p_T jets is twofold: test the QCD predictions and look for Physics beyond the Standard Model. Since the parton scattering is practically an elementary QCD process, the jet distributions can be calculated from first principles, provided that reasonable hadronization modeling is available. Therefore, the high p_T jets serve as a direct test of perturbative QCD (pQCD). Also, their production is sensitive to the strong coupling constant α_S and precise knowledge of the jet cross section can help reduce the uncertainties of the parton distribution functions (PDFs) of the proton. Particularly important is the constraint of the gluon PDF at high momentum fraction. In general, the reduction of the PDFs' uncertainties will be critical for LHC studies looking for Physics beyond the Standard model. However, it should be noted that PDFs' constraints can only be achieved with small theoretical and systematic uncertainties and in that sense it will take considerable amount of time for LHC experiments to collect enough data ($\mathcal{O}(1000\,\text{fb}^{-1})$) to reach the Tevatron experiments' precision. High p_T jets are furthermore sensitive to new Physics (e.g quark compositness, resonances) and given the much higher reach in p_T at LHC with respect to the Tevatron, current limits can be improved and discoveries are possible even at startup.

1.2 MC Samples

The measurements presented in this note are performed with Monte Carlo samples produced for the CMS Combined Software and Analysis Challenge 2008 (CSA08). The events were generated with PYTHIA [8], modeling proton-proton collisions at $\sqrt{s} = 10\,\text{TeV}$ while the interaction of particles with the CMS detector was simulated with the CMS software version CMSSW_2_0_7 which is based on Geant4 [1]. Tune D6T was used in order to model underlying event and multiple interactions. The reconstruction software takes into account the "S156" set of alignment and calibration constants, which contain deviations from the ideal geometry of the detector according to the expectation for $10\,\text{pb}^{-1}$ of data. The samples used here were designed to mimic single jet trigger data sets. For this purpose, they were produced as inclusive samples with low momentum transfer ($\hat{\text{p}}_\text{T}$) threshold at parton level. The details are summarized in Table 1.

1.3 Jet Algorithms

Jets are reconstructed using both the k_T [2],[3] and the SISCone [4] clustering algorithms, with large jet size parameters of $\text{D} = 0.6$ and $\text{R} = 0.7$ respectively which are suitable for QCD dijet events. Both algorithms are infrared- and collinear-safe which is a necessary prerequisite for theoretical calculations. The measurement of the

Sample	MIN $\hat{p}_T$ (GeV)	Events	$\sigma(nb)$	Luminosity (pb^{-1})
JetET20	30	$3,951,200$	$109,100$	0.04
JetET30	45	$4,132,800$	$21,710$	0.19
JetET50	75	$4,007,000$	$2,556$	1.6
JetET80	120	$2,780,200$	318.3	8.7
JetET110	160	$3,852,000$	83.42	46.2
JetET150	220	$4,174,800$	17.81	234

Table 1: Characteristics of the MC samples used in the analyses.

inclusive jet cross section as a function of jet p_T is performed with both algorithms, while all other measurements are carried out with SISCone only.

In the context of this note, we define the particle jets (GenJets) as the jets arising after applying the jet finding algorithms to the stable particles and the calorimeter jets (CaloJets) as the products of the jet finding algorithms when applied to the CMS calorimeter energy depositions.

1.4 Jet Energy Scale

Due to the non-linear calorimeter response, the measured jet energy is lower than the particle jet energy and therefore needs to be corrected. The plan for the jet corrections in CMS is described in [5] and is based on a factorized approach where different levels of corrections are applied sequentially to correct for different effects. The default jet corrections include:

1. Offset (corrects for noise and pile-up energy).
2. Relative (corrects for the η dependence).
3. Absolute (corrects for the p_T dependence).

With the current default reconstruction thresholds (SchemeB), the offset correction is negligible and only the other two (relative, absolute) are applied to jets. According to the plan, data driven techniques will be applied to determine the jet energy corrections when enough collision data will be available. However, at startup, the jet corrections will be derived from MC using MC truth information. The detailed description of the MC truth method for deriving the jet corrections can be found in [20].

Since the analysis topics presented here focus on the startup data, the MC truth jet corrections have been used. The size of the absolute (p_T dependence) jet correction is illustrated in Figure 1 while the closure of the applied corrections is illustrated in Figure 2 where the consistency of the method is proven.

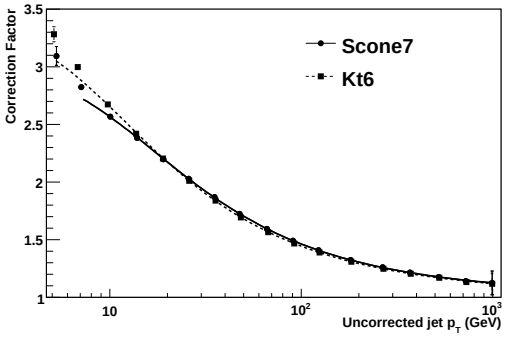

Figure 1: Absolute jet energy correction as a function of the measured calorimeter jet p_T for jet algorithms SISCone R=0.7 and k_T D=0.6.

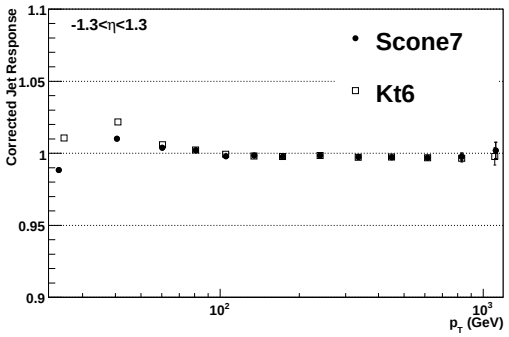

Figure 2: Corrected jet response in the barrel ($|\eta| < 1.3$), as a function of the corrected jet p_T, for jet algorithms SISCone R=0.7 and k_T D=0.6.

1.5 Jet p_T Resolution

The jet p_T resolution can be measured either using the Monte Carlo Truth information or by using collision data. The various methods are described in detail in [23]. For the analysis topics presented in this note, the Monte Carlo

Truth resolution has been used after validating its agreement with the data-driven method. The MC truth jet p_T resolution is obtained from the distribution of the ratio p_T/p_T^{gen} where p_T and p_T^{gen} are the transverse momenta of the (corrected) calorimeter jet and the particle jet respectively. The imposed event selection criteria are listed below:

- the two leading jets are required to be "back-to-back" in ϕ ($\Delta\phi > 2.7$),
- soft third jet (if any) by requiring $p_T^{3rd\ jet} < 10\,\text{GeV}$,
- $p_T^{dijet} > 5\,\text{GeV}$,
- matched calorimeter jets to particle jets, within a cone in the $\eta - \phi$ plane with radius $\Delta R < 0.25$.

where $p_T^{dijet} = (p_T^{jet1} + p_T^{jet2})/2$ and $\Delta R = \sqrt{(\Delta\eta)^2 + (\Delta\phi)^2}$. The corrected response distributions are fitted with a Gaussian to determine the σ which is a measure of the fractional jet p_T resolution.

The method to determine the jet p_T resolution directly from data is called "*Asymmetry method*" and is based on the principle of transverse momentum conservation. After the jets are corrected for jet energy scale (JES), the fundamental observable A (assymetry) is recorded in bins of p_T^{dijet}:

$$A = \frac{p_T^{jet1} - p_T^{jet2}}{p_T^{jet1} + p_T^{jet2}} \tag{1}$$

where p_T^{jet1} and p_T^{jet2} are the transverse momenta of the two leading jets in the event. The assymetry distribution then is fitted with a Gaussian and the resolution is obtained from the following equation:

$$\frac{\sigma(p_T)}{p_T} = \sqrt{2}\,\sigma(A) \tag{2}$$

Events are required to contain at least two jets, with the two leading jets back-to-back in ϕ. In order to correct for additional soft radiation, A is derived for various cuts on the p_T of the third highest jet in p_T, p_T^{jet3} and then extrapolated to the value $p_T^{jet3} = 0$. The final resolution is obtained as a function of the (corrected) jet p_T, parametrized as:

$$\frac{\sigma(p_T)}{p_T} = \sqrt{C^2 + \frac{S^2}{p_T} + \frac{N^2}{p_T^2}} \tag{3}$$

In Figure 3 the MC truth jet p_T resolution is compared to the data-driven one. The observed discrepancy at low

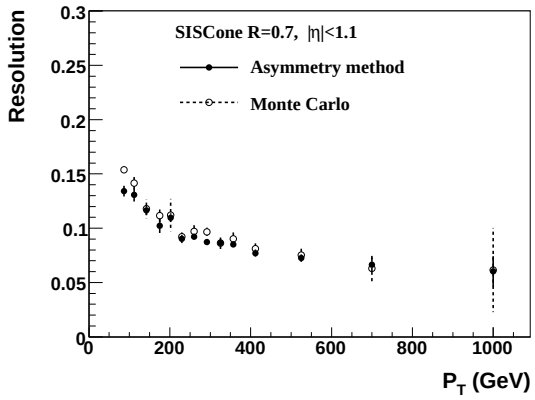

Figure 3: Jet p_T resolution in the barrel ($|\eta| < 1.1$): comparison between MC truth and data-driven method.

p_T is attributed to the non-Gaussian tails of the MC truth response distributions and to the different treatment in MC truth of the additional jets due to soft radiation.

Pseudo-rapidity	C	S	N
$\|\eta\| < 1.1$	0.047	1.4	7.8
$1.6 < \|\eta\| < 2.7$	0.055	1.2	7.7
$3.0 < \|\eta\| < 5.0$	0.082	0.51	5.8

Table 2: MC truth jet $\mathrm{p_T}$ resolution parametrization constants derived from the fit, for the jet algorithm SISCone R=0.7.

1.6 Dijet Mass Resolution

In contrast to the jet $\mathrm{p_T}$ resolution, the dijet mass resolution can not be measured with a data driven method. In order to estimate this quantity (which is necessary for the unsmearing of the dijet mass cross section) one can either use the jet $\mathrm{p_T}$ resolution or extract it directly from MC truth. More specifically, from Equation 20, the dijet mass resolution can be associated to the jet $\mathrm{p_T}$ resolution, neglecting angular effects:

$$\frac{\sigma(M)}{M} = \frac{1}{\sqrt{2}} \frac{\sigma(\mathrm{p_T})}{\mathrm{p_T}} \tag{4}$$

Taking $\mathrm{p_T} \approx M/2$, the resulting dijet mass resolution is $\sigma(M) \approx \sqrt{2}\ \sigma_{p_T}(M/2)$. Alternatively, the MC truth information can be used to derive the dijet mass resolution and validate the previous, approximate expression. For this purpose, the particle dijet mass M^{gen} is constructed from the leading particle jets (GenJets) and the calorimeter dijet mass M from the leading calorimeter jets corrected for the jet energy scale (Corrected Jets). After applying identical event selection cuts, the quantity $M/M^{gen} - 1$ is recorded in bins of M^{gen} and the resulting distributions are fitted with a Gaussian in the range $\pm 1.5\sigma$ around the peak (Figure 4). Finally, the relative dijet mass resolution as a function of M is fitted with a smooth function of the form:

$$\frac{\sigma(M)}{M} = \sqrt{C^2 + \frac{S^2}{M} + \frac{N^2}{M^2}} \tag{5}$$

The values calculated from the fit are: $C = 0.0315 \pm 0.0005$, $S = 1.506 \pm 0.004$, $N \approx 0$. In Figure 5, the direct MC truth measurement is compared to the approximate calculation using the jet $\mathrm{p_T}$ resolution. The two methods are in agreement for dijet masses $M > 200\,\mathrm{GeV}$.

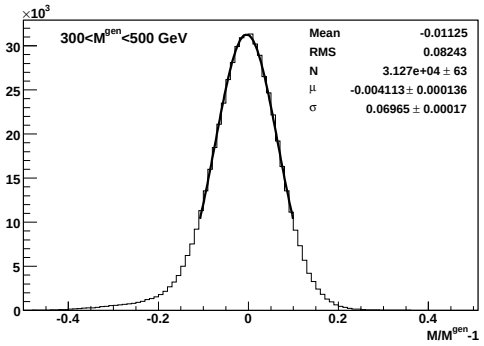

Figure 4: Dijet mass response from MC truth, in a M^{gen} bin, fitted with a Gaussian in the range $\pm 1.5\sigma$ around the peak. The event selection cuts applied are: $|\eta_1|, |\eta_2| < 1.0,\ |\cos\theta^*| < 0.67$.

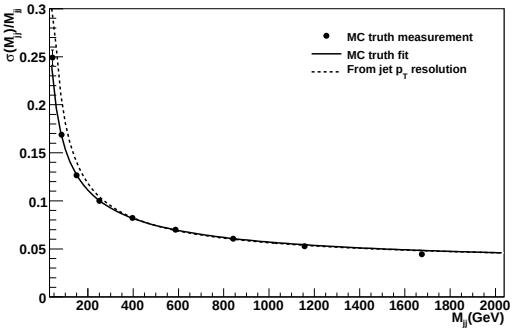

Figure 5: Dijet mass resolution as a function of M. The measurement points are fitted with a smooth function (Equation 5, solid curve) and compared to the approximate calculation using the jet $\mathrm{p_T}$ resolution (dashed line). The event selection cuts applied are: $|\eta_1|, |\eta_2| < 1.0,\ |\cos\theta^*| < 0.67$.

1.7 Event Cleanup and JetID

In a perfect detector and experimental conditions, the measured jets originate from real parton interactions. However, during the actual data taking, energy depositions in the CMS calorimeters from other sources (beam halo, noise, cosmics) can be reconstructed as jets. The rate of such jets is expected to be very small in general but it might be significant for high $\mathrm{p_T}$ jets.

In order to identify and exclude jets with other origin than parton hard scattering, event cleanup and jet ID criteria must be applied. Previous studies [22] indicate that the most significant event cleanup criterion is a cut on the quantity $\not{\mathrm{E}}_\mathrm{T} / \sum \mathrm{E_T}$ where $\not{\mathrm{E}}_\mathrm{T}$ is the missing reconstructed transverse energy and $\sum \mathrm{E_T}$ is the total reconstructed

transverse energy in the event. In a hard parton scattering event, transverse momentum is conserved and no $\not\!\!E_T$ is expected other than jet mismeasurement which is typically a small fraction of $\sum E_T$. Such a cut has been applied in QCD related measurements in the past and while it is very efficient in removing events which contain jets from noise, beam halo or cosmic activity, at the same time its efficiency on real QCD events is almost 100%.

At the same time, specific jet ID cuts, related to jet properties (e.g, electromagnetic energy fraction, number of tracks associated with a jet) are being studied and can been used in addition. Finally, event timing is also being explored.

In the context of this note, no event cleanup or jet ID has been applied since the analyses are performed on MC samples which only contain real QCD events.

2 Inclusive Jet Cross Section

One of the most imporant QCD measurements is the inclusive jet cross section as a function of jet p_T which serves as a test of the theory and at the same time is sensitive to new physics [21]. At LHC's 10 TeV p-p collisions, the jet p_T reach expected will be far beyond the limits of current experiments, thus probing the TeV scale of QCD. It should be emphasized though that this measurement is very sensitive to jet energy scale uncertainties and therefore cannot be used as a precision measurement, at least not until several fb^{-1} of data are accumulated by CMS.

The theoretical, Lorentz invariant, expression for the inclusive jet cross section is given by:

$$E\frac{d^3\sigma}{dp^3} \tag{6}$$

For all practical purposes though, the quantity measured experimentally is the double differential cross section:

$$\frac{d^2\sigma}{dp_T dy} \tag{7}$$

which is related to the theoretical expression as follows:

$$E\frac{d^3\sigma}{dp^3} = \frac{d^3\sigma}{d^2p_T dy} = \frac{1}{2\pi p_T}\frac{d^2\sigma}{dp_T dy} \tag{8}$$

assuming azimuthal symmetry.

2.1 Data-like Spectrum Construction

The differential inclusive jet cross section is measured in bins of transverse momentum and rapidity and is defined as:

$$\frac{d^2\sigma}{dp_T dy} = \frac{C_{unsm}}{\mathcal{L}\cdot\epsilon}\cdot\frac{N_{jets}}{\Delta p_T\cdot\Delta y} \tag{9}$$

where:

- N_{jets} is the number of jets counted in a bin,
- $\mathcal{L}$ is the integrated luminosity,
- ϵ is the efficiency of the event cleanup and ID cuts,
- C_{unsm} is the unsmearing correction factor,
- Δp_T and Δy are the p_T and rapidity bin sizes respectively.

According to Table 1 the number of events generated in each MC sample correspond to different luminosity. This behaviour is similar to the real data taking where prescales will be applied and the accumulated data from each trigger will correspond to different integrated luminosity. Thus, in this note, the luminosity normalization constants are called prescales. The starting point of the measurement is jet counting in (corrected) p_T and rapidity bins (Figure 6). Then the jet p_T spectrum in each rapidity bin is constructed by proper contribution of each sample. The construction is done in three steps:

1. Measurement of the luminosity normalization (prescale) factor: although the prescale factor for each sample is in principle known, it is confirmed by dividing the number of jets vs p_T measured with a particular sample with the same distribution from the highest threshold sample (JetET150) which is always un-prescaled (reference luminosity). The inverse of the plateau of the resulting ratio (Figure 7) gives the prescale factor.

2. Construction of the turn-on curves: in order to identify the p_T values where each sample becomes fully efficient ($> 99\%$), the number of jets vs p_T measured with a particular sample (corrected for the prescale, Figure 8) is divided with the same distribution from the sample with next lower threshold (e.g JetET30/JetET20) also corrected for the prescale. Provided that the tresholds are carefully chosen to allow for sufficient overlap, the resulting distribution has a plateau at unity (Figure 9) which can be fitted by a simple curve: $\epsilon(p_T) = 0.5 \cdot [1 + \mathrm{Erf}(a \cdot p_T)]$. Finally the turn-on point p_T^{th} is defined from the condition $\epsilon(p_T^{th}) = 0.99$. The turn-on point for the lowest threshold sample (JetET20) is determined by comparison to the MinBias jet p_T spectrum.

3. Combined spectrum: the final number of jets in each p_T bin is taken from the highest threshold sample that is efficient, corrected for the corresponding prescale. Thus, only one sample contributes to each p_T bin, avoiding jet double counting in the overlapping regions between samples.

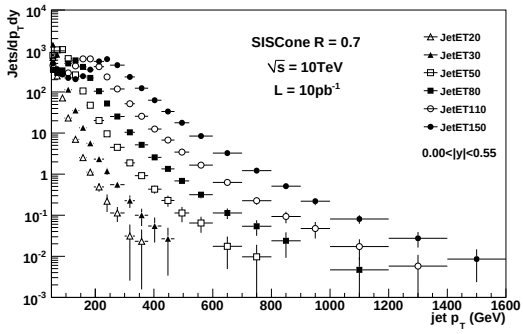

Figure 6: Measured number of jets from each sample in the central rapidity bin.

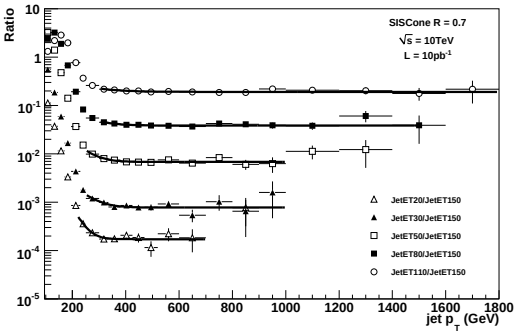

Figure 7: Luminosity normalization: a data driven method to measure the prescale factors.

Sample	JetET20	JetET30	JetET50	JetET80	JetET110	JetET150
MC prescale	5850	1232	146	26.9	5.1	1
Measured prescale	5798 ± 436	1292 ± 88	147 ± 3	25.8 ± 0.4	5.23 ± 0.05	1

Table 3: Comparison between measured and theoretical prescale factors.

Sample	$\lvert y\rvert < 0.55$	$0.55 < \lvert y\rvert < 1.1$	$1.1 < \lvert y\rvert < 2.3$	$2.3 < \lvert y\rvert < 3.0$	$3.0 < \lvert y\rvert < 5.0$
JetET20	80	80	80	80	80
JetET30	120	120	120	106	99
JetET50	196	193	198	169	158
JetET80	248	242	243	220	216
JetET110	307	306	307	282	284
JetET150	392	390	391	347	369

Table 4: Turn on points: jet p_T (in GeV) above which each sample is at least 99% efficient with respect to the sample with next lower threshold.

2.2 Unsmearing

The measured inclusive jet cross section vs p_T is the convolution of the actual particle jet spectrum, folded with the detector finite p_T and y resolutions. While the effect of the y resolution can be neglected to first order, the p_T smearing effect must be corrected for. The unsmearing corrections for the jet p_T spectra in these studies are derived using the *Ansatz Method*, which is described below.

The starting point is a functional description of the unknown particle jet cross section:

$$f(p_T) = N \cdot p_T^{-a} \cdot (1 - x_T)^b \cdot \exp(-\gamma x_T) \tag{10}$$

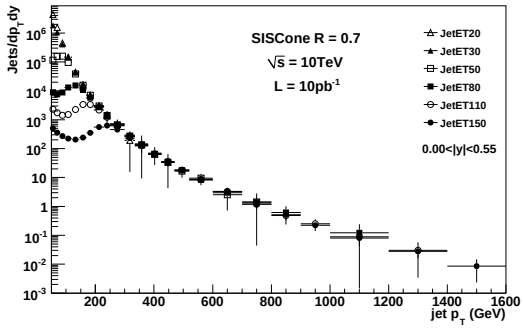

Figure 8: Inclusive jet $\mathrm{p_T}$ distributions in the central rapidity bin, corrected for prescale.

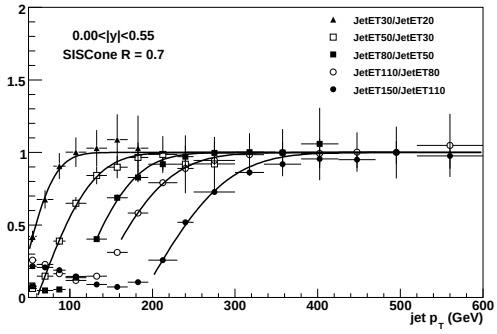

Figure 9: Sample relative efficiency for the central rapidity bin.

where $\mathrm{x_T} = 2\mathrm{p_T}/\sqrt{s}$. The particular function is theoretically motivated (the $(1-\mathrm{x_T})^b$ term reflects the PDF behaviour at high $\mathrm{x_T}$ and the $\mathrm{p_T}^{-a}$ imitates the QCD matrix element). The measured cross section is defined as the convolution of the particle jet spectrum with the detector resolution:

$$F(\mathrm{p_T}) = \int_0^\infty f(\mathrm{p'_T}) R(\mathrm{p'_T}, \mathrm{p_T}) d\mathrm{p'_T} \tag{11}$$

In order to apply this method it is necessary to model the $\mathrm{p_T}$ resolution, the simplest assumption being the Gaussian approximation:

$$R(\mathrm{p'_T}, \mathrm{p_T}) = \frac{1}{\sqrt{2\pi}\sigma(\mathrm{p'_T})} \exp\left[-\frac{(\mathrm{p'_T}-\mathrm{p_T})^2}{2\sigma^2(\mathrm{p'_T})}\right] \tag{12}$$

where $\sigma(\mathrm{p_T})$ is defined in Equation 3.

Although the Gaussian model for the resolution is reasonable enough, it fails to describe the full shape (tails). Due to the steeply falling nature of the inclusive jet $\mathrm{p_T}$ spectrum, the mis-modeling of the resolution tails introduces a systematic bias on the unsmearing correction.

Once the measured spectrum is fitted with the smeared Ansatz function, the unsmearing correction (multiplicative factor) is calculated for every bin as:

$$C_{bin} = \frac{\int_{bin} f(\mathrm{p_T}) d\mathrm{p_T}}{\int_{bin} F(\mathrm{p_T}) d\mathrm{p_T}} \tag{13}$$

In Figure 10 the measured cross sections in different rapidity bins are fitted successfully with the smeared ansatz function as indicated by the fit quality plots (Figure 11). The final unsmearing correction factors are shown in Figure 12 where it can be seen that the unsmearing correction becomes larger for higher rapidities. This is due to the much steeper falling spectrum, despite the fact that the resolution is better with respect to central rapidities.

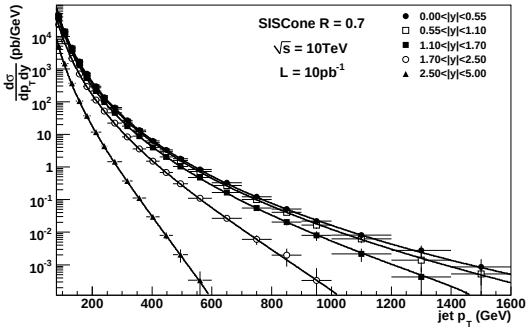

Figure 10: Measured inclusive jet cross section vs $\mathrm{p_T}$ for different rapidity ranges, fitted with the smeared ansatz function.

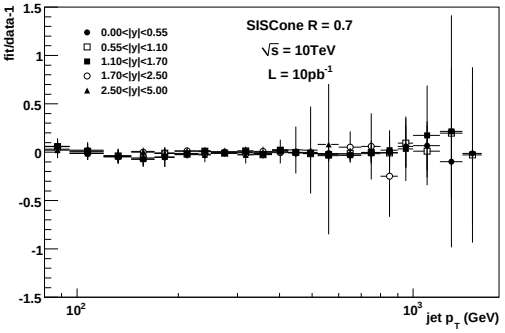

Figure 11: Quality of the fit: fractional difference between the fitting curve and the "data" points.

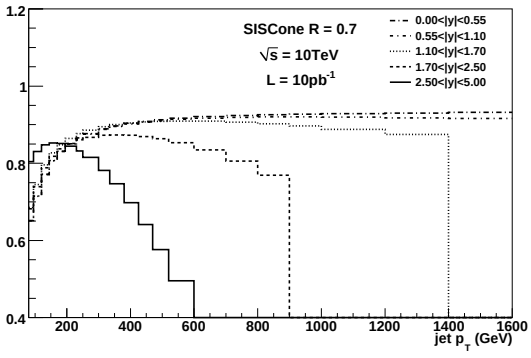

Figure 12: Unsmearing correction factors for different rapidity ranges.

2.3 Experimental Systematic Uncertainties

The dominant sources of systematic uncertainties for the cross section measurement are the jet energy scale (JES) and the luminosity while non negligible contribution comes from the jet energy and jet angular resolutions. Due to the fact that the analysis presented here is targeting the first $10\,\mathrm{pb}^{-1}$ of data taking, it becomes clear that the JES uncertainty is by far the dominant one.

The inclusive jet cross section measurement is sensitive to the JES because it is expressed as a function of the corrected jet $\mathrm{p_T}$ and due to the steeply falling nature of the spectrum. A rough estimate of the dependence of the cross section uncertainty on JES can be obtained from the approximate expression $d\sigma/d\mathrm{p_T} \sim \mathrm{p_T}^{-a}$ which yields the uncertainty as:

$$\frac{\delta(d\sigma/d\mathrm{p_T})}{d\sigma/d\mathrm{p_T}} \sim -a\frac{\delta\mathrm{p_T}}{\mathrm{p_T}} \tag{14}$$

Given that $a \sim 10$ it is easily calculated that a 10% JES uncertainty is translated in $> 100\%$ uncertainty in the jet cross section. In the context of the analysis presented here, two different scenarios for the JES uncertainty have been examined:

- Scenario 1: (flat JES uncertainty) according the studies performed in the CMS JetMET group, a flat 10% JES uncertainty is the best educated guess for the startup of the experiment [5].
- Scenario 2: (linearly increasing JES uncertainty) the JES uncertainty is assumed to be 10% at $100\,\mathrm{GeV}$ linearly increasing up to 20% at $2\,\mathrm{TeV}$. This scenario is very pessimistic and partially motivated by previous experiments experience where the JES uncertainty appeared to increase with increasing jet $\mathrm{p_T}$.

One way to treat the JES uncertainty is to vary explicitly the jet calibration constant, according to each scenario, on a jet by jet basis and repeat the cross section measurement. However, although this method is straightforward, it suffers from the statistical fluctuations, especially at higher $\mathrm{p_T}$. Alternatively, one can use the smeared ansatz function which has been fitted to the measured spectrum (Equation 11). Each jet $\mathrm{p_T}$ bin is determined by its boundary values $\mathrm{p_T^l}$, $\mathrm{p_T^h}$ and the measured cross section is:

$$\left(\frac{d^2\sigma}{d\mathrm{p_T}dy}\right)_{bin} = \frac{1}{\mathrm{p_T^h} - \mathrm{p_T^l}} \int_{\mathrm{p_T^l}}^{\mathrm{p_T^h}} F(\mathrm{p_T})d\mathrm{p_T} \tag{15}$$

For shifted jet $\mathrm{p_T}$ values due to the JES uncertainty, the measured cross section is:

$$\left(\frac{d^2\sigma}{d\mathrm{p_T}dy}\right)^{\pm}_{bin} = \frac{1}{\mathrm{p_T^h} - \mathrm{p_T^l}} \int_{\left[1\pm\delta(\mathrm{p_T^l})\right]\mathrm{p_T^l}}^{\left[1\pm\delta(\mathrm{p_T^h})\right]\mathrm{p_T^h}} F(\mathrm{p_T})d\mathrm{p_T} \tag{16}$$

where $\delta(\mathrm{p_T})$ is the JES uncertainty according to the particular scenario. Using the above results the fractional systematic uncertainty of the jet cross section is:

$$\alpha(\pm) = \frac{\left(\frac{d^2\sigma}{d\mathrm{p_T}dy}\right)^{\pm}_{bin}}{\left(\frac{d^2\sigma}{d\mathrm{p_T}dy}\right)_{bin}} - 1 \tag{17}$$

In Figures 13 and 14 the fractional systematic uncertainties are shown for both JES scenarios, in two different rapidity bins, in comparison to the statistical errors. The uncertainty of the cross section appears to grow for higher rapidities, the reason being that the spectrum becomes more steeply falling.

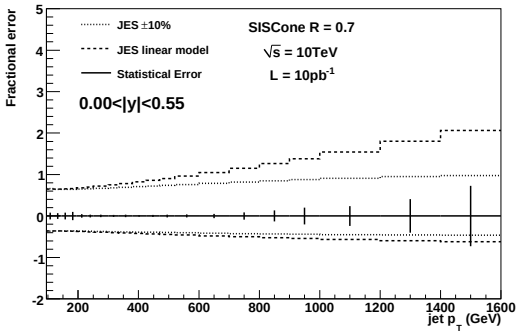

Figure 13: Comparison between the dominant systematic uncertainty (JES) and the statistical errors in the central rapidity bin.

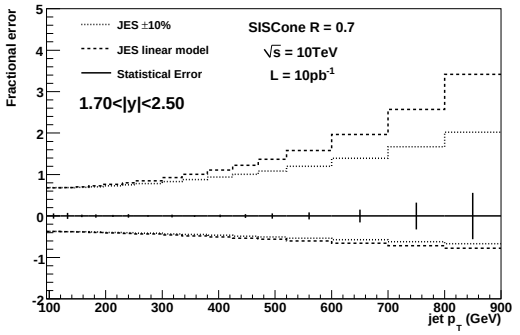

Figure 14: Comparison between the dominant systematic uncertainty (JES) and the statistical errors in the rapidity bin in the Endcap region.

2.4 Comparison to Theory

Within the limited scope of this exercise the aim was to go once through the whole chain of analysis steps necessary to confront measured inclusive jet cross sections with theory predictions. This section describes the employed ingredients on the theory side. A complete derivation of all associated uncertainties was not attempted. This is the subject of further studies which are currently in progress.

2.4.1 NLO Calculation and PDF Uncertainties

Within the timeline of an experiment there are usually two stages for comparing measured inclusive jet cross sections to theoretical predictions. At first, with a rather limited experimental precision, calculations of perturbative QCD of at least next-to-leading order will be considered as definite prediction to which the measurement is compared for consistency ... or for the observation of discrepancies, especially at highest transverse momenta. The parton density functions (PDFs) of the proton and the coupling of the strong interaction α_S, which themselves are based on results of other experiments, are taken as input. This is also the case here. Solely, the uncertainty derived for the employed PDFs from the experimental inputs has been evaluated. Fitting PDFs and/or α_S as possible later on with more data and smaller experimental systematic uncertainties was out of scope of this early analysis exercise.

For the NLO calculation the program NLOJET++ [6] is employed which would be completely sufficient for a simple comparison. Nevertheless, as a preparation for future PDF fits, a more efficient set-up in the form of the fastNLO project [7] is used. There, the very time consuming step of a precise jet cross section computation in NLO is done only once. At the expense of interpolating the PDFs between fixed support points in fractional proton momentum x the PDF dependency can be separated from the hard matrix element calculation and a rederivation of the considered cross section for arbitrary input PDFs and α_S values can be done quickly.

The simulated MC event samples representing the data in this exercise have been generated with the D6T tune for PYTHIA, an update to the tune DWT [9], and employed the CTEQL1 leading-order PDF set [10]. The corresponding NLO set is CTEQ6M which was therefore adopted for the central NLO calculations. In order to have more recent estimates for the PDF uncertainty though, the CTEQ65 [11] fits were used from which the uncertainty has been derived according to the prescription given in [10]. In all cases the default value and evolution was taken for α_S as defined by the corresponding PDF set.

2.4.2 Corrections for Hadronization and the Underlying Event

As a further point it has to be remembered that NLO calculations can not be compared directly to calibrated calorimeter jets. In addition, the influence of the parton shower, hadronization and decays as well as the Underlying Event has to be taken into account and correction factors have to be applied to the NLO result. Unfortunately, this can not yet be done in a completely consistent manner since most MC generation programs, do only allow for LO

matrix elements to be coupled to parton showers and the subsequent hadronization. An exception to this rule is MC@NLO [12, 13], however, the QCD process which is required for inclusive jets is not yet implemented.

Keeping this in mind, the subsequent procedure was followed in order to estimate this correction. It is assumed that the partonic final state, i.e. all partonic like objects (gluons, quarks, anti-quarks, diquarks) that enter into the string fragmentation phase of PYTHIA, is sufficiently close to NLO such that corrections derived from it are also applicable to NLO. Hence, the inclusive jet cross sections have been derived from PYTHIA once for the partonic final state without Underlying Event and once for the hadronic final state, i.e. all stable particles, including the Underlying Event. The ratio of the latter to the former is then multiplied with the NLO jet cross section. The final results are shown as theory reference in Figures 16, 17, 15 and 22 together with the corresponding PDF uncertainties.

In order to be less model dependent this procedure should be repeated using alternative MC generators, e.g. HERWIG employing the cluster instead of the string fragmentation model for hadronization, and different Underlying Event tunes. Work to derive a systematic uncertainty by comparing the corrections for PYTHIA (with the D6T tune), HERWIG+JIMMY [14, 15, 16] and HERWIG++ [17, 18, 19] are under way.

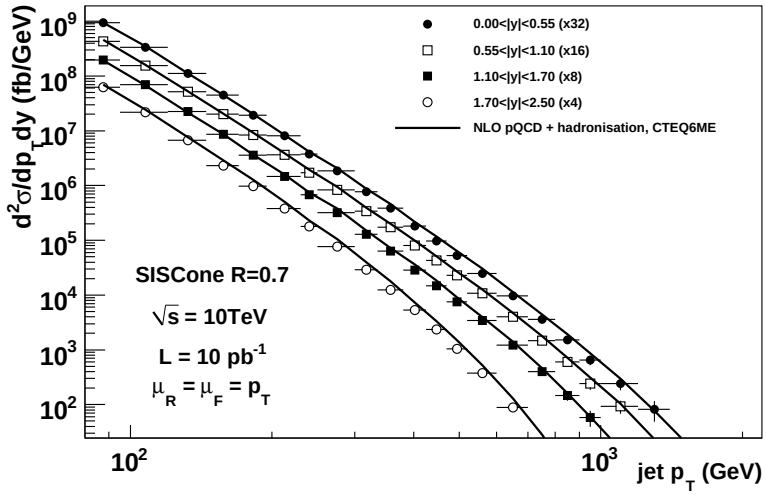

Figure 15: Measured inclusive jet cross section in different rapidity bins, corrected for smearing effects, in comparison to theoretical predictions, for the jet algorithm SIScone R=0.7.

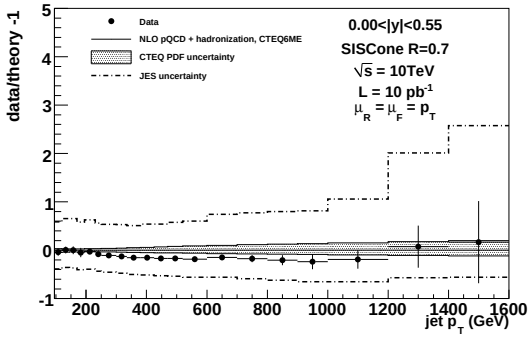

Figure 16: Fractional difference between the measured inclusive jet cross section as a function of p_T and the theory (pQCD+hadronization) in the central rapidity, for the jet algorithm SIScone R=0.7. The JES and the PDF uncertainties are also shown.

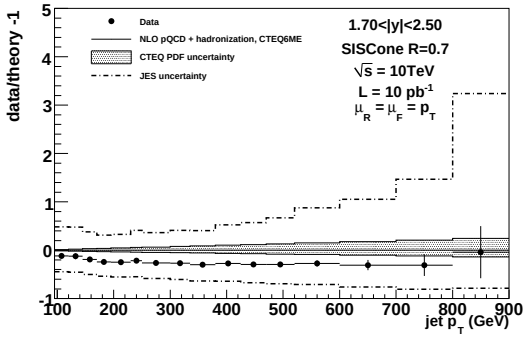

Figure 17: Fractional difference between the measured inclusive jet cross section as a function of p_T and the theory (pQCD+hadronization) in the rapidity bin in the Endcap, for the jet algorithm SIScone R=0.7. The JES and the PDF uncertainties are also shown.

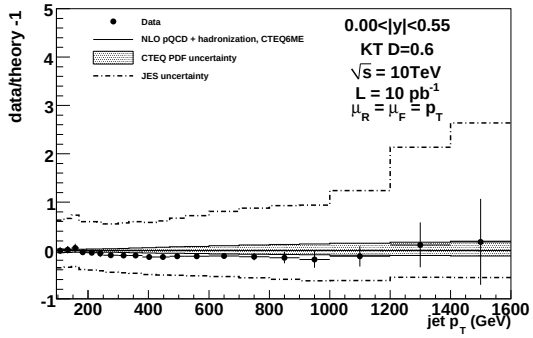

Figure 18: Fractional difference between the measured inclusive jet cross section as a function of p_T and the theory (pQCD+hadronization) in the central rapidity, for the jet algorithm k_T D=0.6. The JES and the PDF uncertainties are also shown.

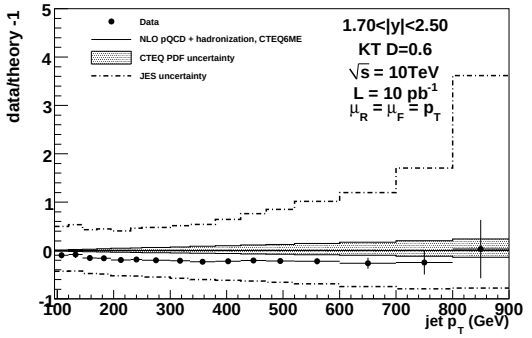

Figure 19: Fractional difference between the measured inclusive jet cross section as a function of p_T and the theory (pQCD+hadronization) in the rapidity bin in the Endcap, for the jet algorithm k_T D=0.6. The JES and the PDF uncertainties are also shown.

2.5 Alternative Spectrum Construction

As the data-driven approach described in Section 2.1 makes it necessary to reject a large amount of the simulated data, an alternative approach is needed to make optimal use of the available MC statistics. Unlike real trigger streams, the simulated events in the overlapping phase-space regions between samples are not identical. Therefore, an alternative approach to construct the spectrum is feasible, making optimal use of the available MC statistics. In order to reconstruct the jet cross section from the MC samples, the integrated cross section given by PYTHIA (Table 1) is used in order to combine the different phase space elements covered by the samples. Additionally, an overlapping matrix is determined in order to estimate the relative weights of the events coming from the samples, in a certain $\hat{p}_T$ region. The final weight is determined from the relation between the number of events in a certain $\hat{p}_T$ bin and the total number of events in the bin when using all events of all samples. Table 5 gives the distribution of the events that were successfully processed, into $\hat{p}_T$ bins. The weight for each jet that belongs to an event

Sample/$\hat{p}_T$ [GeV]	$30-45$	$45-75$	$75-120$	$120-160$	$160-220$	>220	Total
JetET20	3.157.005	707.054	83.251	8.901	2.303	686	3.959.200
JetET30	0	3.642.339	429.007	45.358	12.676	3.420	4.132.800
JetET50	0	0	3.507.243	368.309	103.455	27.993	4.007.000
JetET80	0	0	0	2.030.797	569.217	154.186	2.754.200
JetET110	0	0	0	0	3.019.120	816.880	3.836.000
JetET150	0	0	0	0	0	4.143.000	4.143.000
Total	3.157.005	4.349.393	4.019.501	2.453.365	3.706.771	5.146.165	22.832.200

Table 5: Distribution of the processed events over the phase space. The columns show the sample composition of each $\hat{p}_T$ bin and the rows show the $\hat{p}_T$ distribution of each sample.

coming from sample i and $\hat{p}_T$ bin j is defined as

$$w_{ij} = \frac{\sigma_i}{N_i}\frac{N_{ij}}{N_j} \tag{18}$$

where σ_i is the integrated cross section of sample i, N_i is the number of events in the same sample, N_{ij} is the number of events in the $\hat{p}_T$ bin j from sample i and N_j is the total number of events in $\hat{p}_T$ bin j from all samples. The N_{ij} are the entries of Table 5, with lines i and collums j.

Using the alternative method described above, one can construct the spectrum from calorimeter jets and apply the same pt resolution unfolding method used for the data-like constructed spectrum (Section 2.2). For the k_T algorithm the energy corrected spectrum and the fitting of the ansatz function are given in Figure 20, the unsmeared spectrum and the unsmearing corrections in Figure 21. Finally the comparison to pQCD derived at NLO and uncertainties from energy scale and pdfs (in the central rapidity bin), are shown in figure 22. The statistical uncertainties in Figure 22 are reduced w.r.t. Figure 18, due to the much more efficient use of the available MC statistics.

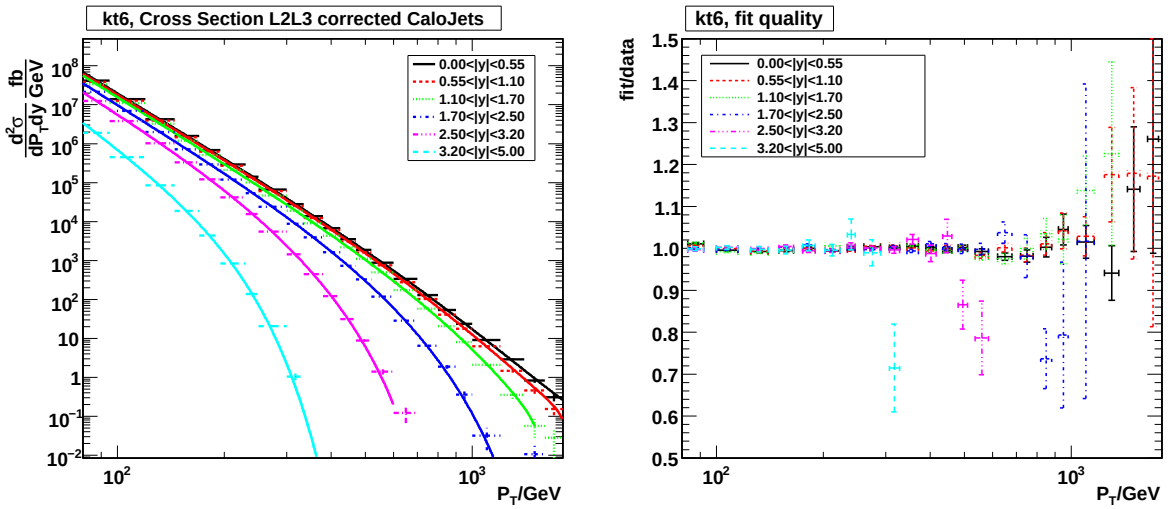

Figure 20: Left: energy corrected spectrum fitted with ansatz function, right: fit quality.

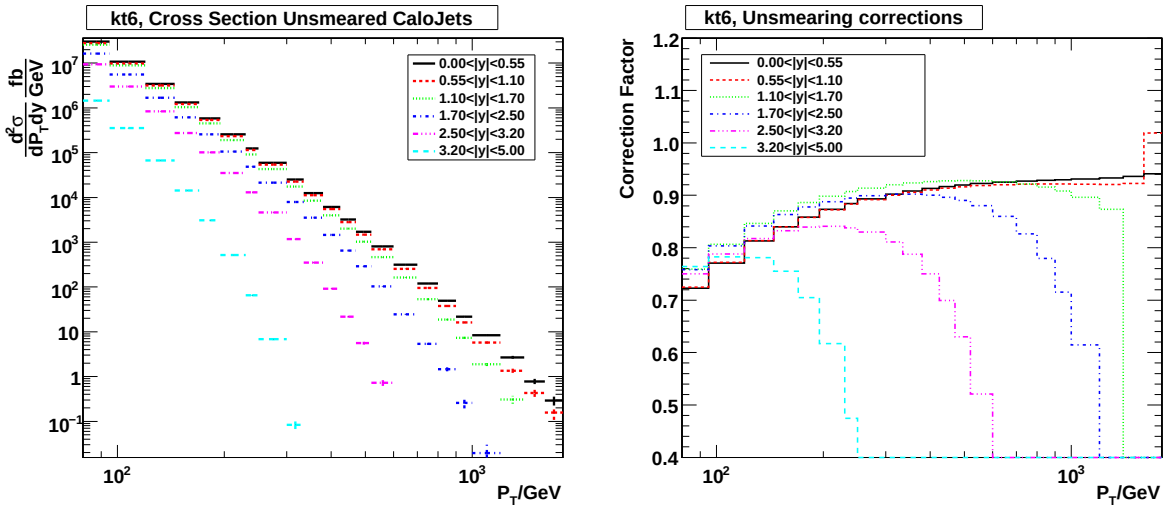

Figure 21: Left: unsmeared spectrum, right: unsmearing correction.

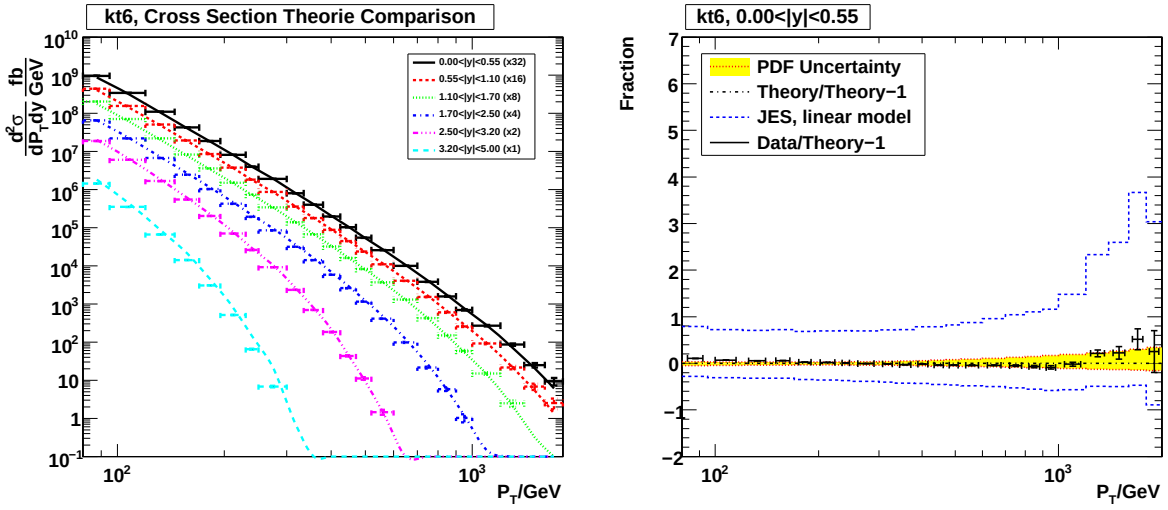

Figure 22: Left: pQCD theory and unsmeared calojets, right: relative comparison in central bin, including energy scale and pdf uncertainties

3 Dijet Mass Cross Section

3.1 Kinematics of the Dijet System

The dijet system in an event is defined as the system of the two leading jets (the two jets with higher $\mathrm{p_T}$, after jet energy corrections have been applied). The dijet mass is formally expressed as:

$$M_{jj}^2 = P_{j_1}^{\mu} P_{\mu,j_2} = (E_1 + E_2)^2 - (\vec{p}_1 + \vec{p}_2)^2 \tag{19}$$

where $P_{j_i}^{\mu} = (E_i, \vec{p}_i)$ are the four-momenta of the two leading jets. In the limit of massless jets, the dijet mass can be expressed in terms of measured jet quantities as

$$M_{jj}^2 = 2p_{T,1}p_{T,2}[\cosh(\eta_1 - \eta_2) - \cos(\phi_1 - \phi_2)] \tag{20}$$

The dijet system can be also described in its center of mass (CM) frame:

$$\eta_{boost} = \frac{1}{2}(\eta_1 + \eta_2) \quad , \quad \eta^* = \frac{1}{2}(\eta_1 - \eta_2) \tag{21}$$

where the Lorentz invariant η^* variable is related to the CM scattering angle:

$$\cos\theta^* = \tanh\eta^* \tag{22}$$

and the η_{boost} variable is the longitudinal boost between the detector frame and the CM frame. At parton level $p_{T,1} = p_{T,2} = \mathrm{p_T} = \mathrm{E_T}$ and $\phi_1 = \phi_2$ while $y_i = \eta_i$ (massless partons) and the scattering cross section is defined as:

$$\frac{d^3\sigma}{d\mathrm{E_T}d\eta_1 d\eta_2} \tag{23}$$

while it can also be expressed in terms of the CM frame variables:

$$\frac{d^3\sigma}{dMdcos\theta^* d\eta_{boost}} \tag{24}$$

For practical purposes, the angular variable χ is used (Equation 25) because the dominant QCD process is "t-channel" (Rutherford like scattering) in which case the cross section in terms of χ is almost flat, allowing for easier comparison between theory and measurement.

$$\chi = e^{2|\eta^*|} = \frac{1 + |\cos\theta^*|}{1 - |\cos\theta^*|} \tag{25}$$

3.2 Event Selection

The dijet invariant mass cross section is measured in a subset of the available phase space and the arguments for the event selection cuts are both theoretical and experimental. For the measurement presented here, the following event selection cuts are used:

- At least 2 jets in the event,
- $|\eta_1|, |\eta_2| < 1$,
- $|\cos\theta^*| < 0.67$.

The restriction for the jets to be contained in the central region ($|\eta| < 1$) is motivated by the fact that this region of the calorimeter is better understood, with little variation of the jet response vs η. The requirement on $|\cos\theta^*|$ is motivated by the fact that in most of the interesting models of Physics beyond the Standard Model, high $\mathrm{p_T}$ jets are created isotropically ("s-channel") in contrast to QCD ("t-channel"). Therefore, by requiring jets at large scattering angles, the sensitivity to new Physics is increased.

3.3 Spectrum Construction

The measurement of the dijet cross section is performed in bins of the invariant dijet mass and is experimentally defined as:

$$\frac{d\sigma}{dM} = \frac{C_{unsm}}{\mathcal{L} \cdot \epsilon} \cdot \frac{N_{events}}{\Delta M} \tag{26}$$

where

- N_{events} is the number of events satisfying the event selection criteria, counted in a bin,
- $\mathcal{L}$ is the integrated luminosity,
- ϵ is the efficiency of the event selection, event cleanup and jet ID cuts,
- C_{unsm} is the unsmearing correction factor,
- ΔM is the mass bin size.

The spectrum is constructed following the same methodology as described in Section 2.1: first the spectra measured by individual data samples are corrected with the measured prescale factors (Table 3), leading to the distributions in Figure 23. Then the relative efficiency of each sample with respect to the sample with next lower threshold is determined by dividing the prescale-corrected spectra (Figure 24) and the 99% efficiency points are extracted by a continuous fit (Table 6). Finally, the spectrum is constructed by using the data of each sample between its turn-on point and the turn-on point of the sample with next higher threshold.

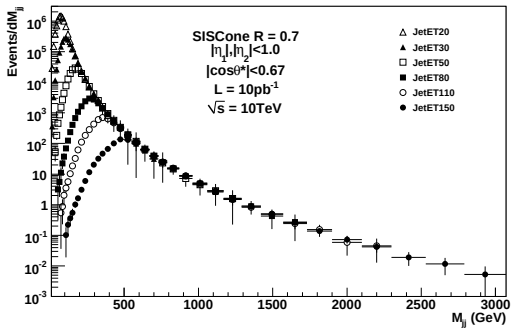

Figure 23: Dijet mass M_{jj} distributions, corrected for prescale.

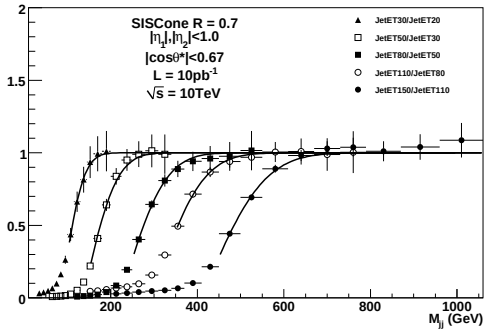

Figure 24: Sample relative efficiency as a function of the dijet mass M_{jj}.

Sample	JetET20	JetET30	JetET50	JetET80	JetET110	JetET150
$M_{jj}(GeV)$	120	184	287	429	528	692

Table 6: Dijet mass M_{jj} turn on thresholds where each sample is at least 99% efficient, for the phase space considered in this measurement.

3.4 Unsmearing

The unsmearing of the dijet mass spectrum is necessary due to the finite mass resolution and is done by using the ansatz function technique as described in section 2.2. The following ansatz function was used:

$$f(M) = N \cdot M^{-a} \cdot \left(1 - \frac{M}{\sqrt{s}}\right)^{b} \tag{27}$$

The mass resolution is approximated by the Gaussian model:

$$R(M, M') = \frac{1}{\sqrt{2\pi}\sigma(M')} \exp\left[-\frac{(M - M')^2}{2\sigma^2(M')}\right] \tag{28}$$

and $\sigma(M)$ is calculated from Equation 5 using the parameters from the fit to the MC truth measurement (Figure 5). The measured (smeared) dijet mass spectrum is fitted with the convolution of the Ansatz function with the resolution:

$$F(M) = \int_0^\infty f(M')R(M', M)dM' \tag{29}$$

and the unsmearing correction is calculated for each bin as:

$$C_{bin} = \frac{\int_{bin} f(M)dM}{\int_{bin} F(M)dM} \tag{30}$$

In Figure 25 the dijet mass spectrum is fitted with the smeared ansatz function with good agreement as indicated in Figure 26.

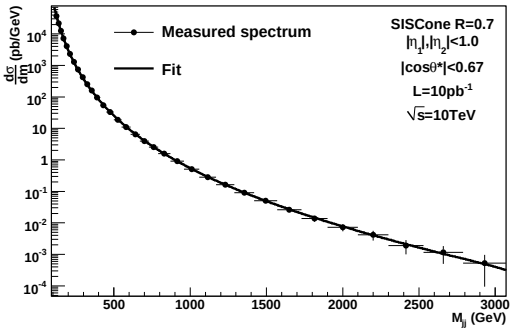

Figure 25: Measured dijet mass cross section fitted with the smeared ansatz function (equation 27). The parameter values from the fit are: $N = (8.4 \pm 1.8) \cdot 10^{14}$, $a = 4.97 \pm 0.04$, $b = 6.9 \pm 0.7$.

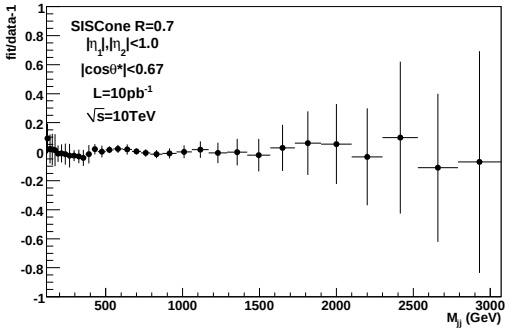

Figure 26: Quality of the fit: fractional difference between the fitting curve and the "data" points.

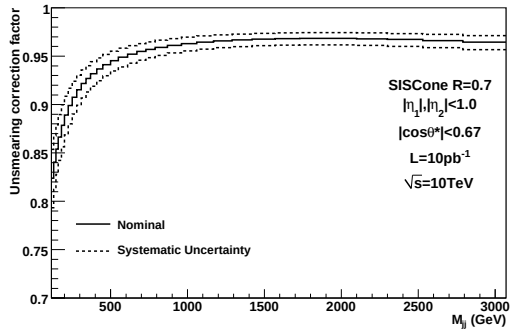

Figure 27: Unsmearing correction due to finite mass resolution. The systematic uncertainty corresponds to 10% uncertainty in the mass resolution.

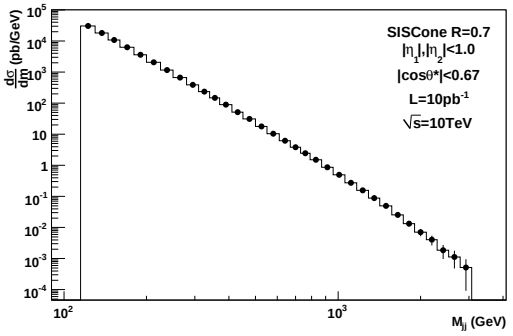

Figure 28: Dijet mass cross section corrected for smearing effects.

3.5 Experimental Systematic Uncertainties

As for the case of the inclusive jet cross section measurement, the dominant experimental systematic uncertainty for the measurement of the dijet mass cross section arises from the JES uncertainty. Due to the steeply falling shape of the mass spectrum, any error on the horizontal axis (mass) is translated into multiple times larger error in the cross section. The analytic way to estimate the dependence of the mass cross section on the JES relies on the continuous fit of the smeared ansatz function on the data; in a mass bin with boundaries M_l and M_h the measured cross section is:

$$\left(\frac{d\sigma}{dM}\right)_{bin} = \frac{1}{M_h - M_l} \int_{M_l}^{M_h} F(M)dM \tag{31}$$

For shifted jet $\mathrm{p_T}$ values due to the JES uncertainty, the dijet mass is also shifted by the amount $\delta(M) \equiv \delta(\mathrm{p_T} = M/2)$ where $\delta(\mathrm{p_T})$ is the JES uncertainty and the measured cross section becomes:

$$\left(\frac{d\sigma}{dM}\right)^{\pm}_{bin} = \frac{1}{M_h - M_l} \int_{[1\pm\delta(M_l)]M_l}^{[1\pm\delta(M_h)]M_h} F(M)dM \tag{32}$$

Using the above results the fractional systematic uncertainty of the dijet mass cross section is calculated as:

$$\alpha(\pm) = \frac{\left(\frac{d\sigma}{dM}\right)^{\pm}_{bin}}{\left(\frac{d\sigma}{dM}\right)_{bin}} - 1 \tag{33}$$

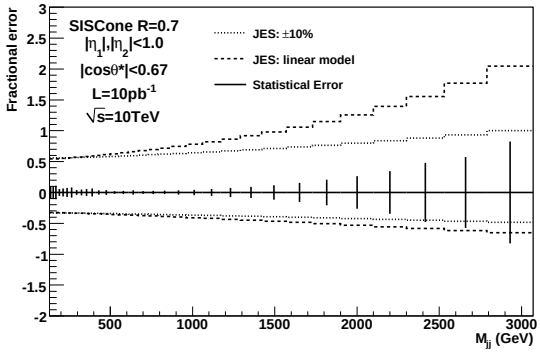

Figure 29: JES systematic uncertainty in the dijet mass cross section.

Another source of experimental systematic uncertainty is related to the assumed dijet mass resolution which affects primarily the unsmearing correction. In Figure 27 there is illustrated the impact of flat 10% variation (independent of mass) of the dijet mass resolution on the unsmearing correction. The resulting uncertainty on the unsmeared cross section is of the order of $\sim 2-5\%$ which is negligible compared to the impact of the JES uncertainty. The resolution uncertainty will become important for a larger data sample and reduced JES uncertainty. Finally, the luminosity uncertainty has apparent implications on the invariant mass cross section but it is merely an overall scale factor, not altering the spectrum shape, which is crucial for resonance searches.

4 Dijet Angular Distributions

Dijet angulars distribution can be used as a probe of physics beyond the Standard Model. In pQCD dijet production is dominated by "t-channel" exchange which results in angular distributions that are peaked in the forward direction. Many models of new physics, however, predict angular distributions that are much more isotropic ("s-channel") than those predicted by pQCD.

4.1 Event Selection

It is convenient to measure the dijet angular distribution in terms of the variable $\chi \equiv e^{2|y^*|} \approx e^{2|\eta^*|}$ (Equation 25) where $y^* = \frac{y_1 - y_2}{2}$ and y_1, y_2 are the rapidities of the two leading jets in the event (Section 3.1). Another useful variable is the average rapidity of the two leading jets, $y^{boost} = \frac{y_1+y_2}{2} \approx \eta_{boost}$. The variables y^* and y^{boost} satisfy the inequality $|y^{boost}| + |y^*| < |y_{max}|$, where y_{max} is the maximum rapidity of an individual jet. For $\chi < 20$, or equivalently $|y^*| < 1.5$, the requirement $|y^{boost}| < 1.5$ constrains the jet rapidities within the HCAL barrel and endcap regions (Figure 30).

Jets are reconstructed using the SISCone jet algorithm with cone size $R = 0.7$. Events are selected from each sample using the data-driven approach described in Section 2.1. Relative sample efficiencies and prescale factors are taken from the inclusive jet analysis and only events where the inclusive jet sample is fully efficient are used in the analysis. Bins of dijet mass M_{jj} are then determined for each dataset such that the acceptance in mass is 100% for $\chi < 20$ (Figure 31) according to the approximate expression $M^2_{jj} = 2\mathrm{p}^2_{\mathrm{T}}[\cosh(\ln\chi) + 1]$ which follows from Equation 20 assuming massless jets, back to back in ϕ.

4.2 Angular Distributions

The experimental observable for the study of the dijet angular distributions is the differential dijet cross section vs χ normalized to the integrated cross section:

$$\frac{1}{\sigma_{dijet}} \frac{d\sigma_{dijet}}{d\chi} \tag{34}$$

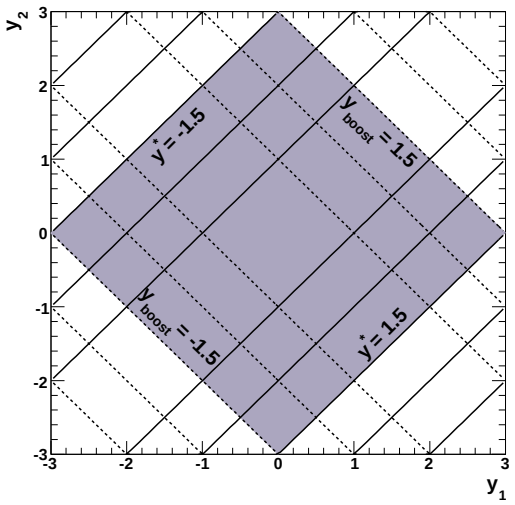

Figure 30: Dijet angular phase space. For $\chi < 20$ (corresponding to $|y^*| < 1.5$), we require $|y^{boost}| < 1.5$ to constrain $|y_1|, |y_2| < 3$.

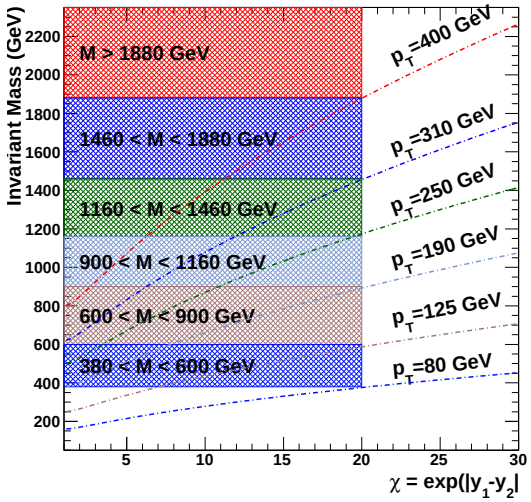

Figure 31: Lines of constant p_T in the mass vs χ plane for massless jets with $p_{T1} = p_{T2}$ and $\Delta\phi = \pi$. The curves shown correspond to the p_T values for each dataset where the sample is fully efficient.

The distributions are shown in Figure 32 for several bins in M_{jj}. The importance of the dijet angular distributions lies in the fact that they are less sensitive to many experimental and theoretical uncertainties which tend to cancel.

The normalized χ distributions have not been corrected for energy or position resolution effects as they are relatively insensitive to these effects. This can be seen in Figure 33, where the ratios of normalized χ distributions from reconstructed calorimeter jets to distributions from particle jets are plotted. These ratios differ from unity at the 0.5% level.

4.3 Systematic Uncertainties

The dominant source of experimental uncertainty arises from the jet energy scale (JES). Although most of the absolute JES uncertainties cancel in the χ shape analysis, variations in the uncertainty across rapidity do not. This analysis uses the pessimistic Scenario 2 JES uncertainties described in Section 2.3, modified to include additional uncertainties for the endcap and forward regions of the detector. For $1.1 < |y| < 2.5$, an additional 10% uncertainty is added for $p_T < 100$ GeV, linearly increasing to 20% at $p_T = 2$ TeV; for $|y| > 2.5$, an additional 15% uncertainty is added for $p_T < 100$ GeV, linearly increasing to 30% at $p_T = 500$ GeV.

The systematic uncertainty in the χ distribution due to JES is shown in Figure 34. For all but the highest M_{jj} bin, the uncertainty varies from ≈20% at low and high values of χ to ≈5% in the middle region. In the highest M_{jj} bin, the uncertainty grows to ≈40% at the high and low edges of the χ distribution.

4.4 Comparison to Theory

The normalized χ distributions are compared to parton level theoretical predictions for several bins in M_{jj} in Figure 35. Comparisons are made to bare LO pQCD predictions and to LO pQCD supplemented with contact interaction terms[33]. Two choices of contact interaction scale are shown, $\Lambda^+ = 3$ and 5 TeV. For these scales, the distributions from the high dijet mass bins show clear sensitivity to new physics arising from contact interactions with only $10\,\text{pb}^{-1}$ of integrated luminosity.

5 Dijet Azimuthal Decorrelation

The QCD radiative processes are particularly important for new physics searches at CMS. A robust way of studying these processes is by measuring the distribution of the azimuthal angle between the two leading jets in a dijet event. To leading order these jets have equal transverse momentum and correlated azimuthal angle (back-to-back, $\Delta\phi = \pi$). In reality however, the dominant parton-parton scattering which leads to the observation of the two

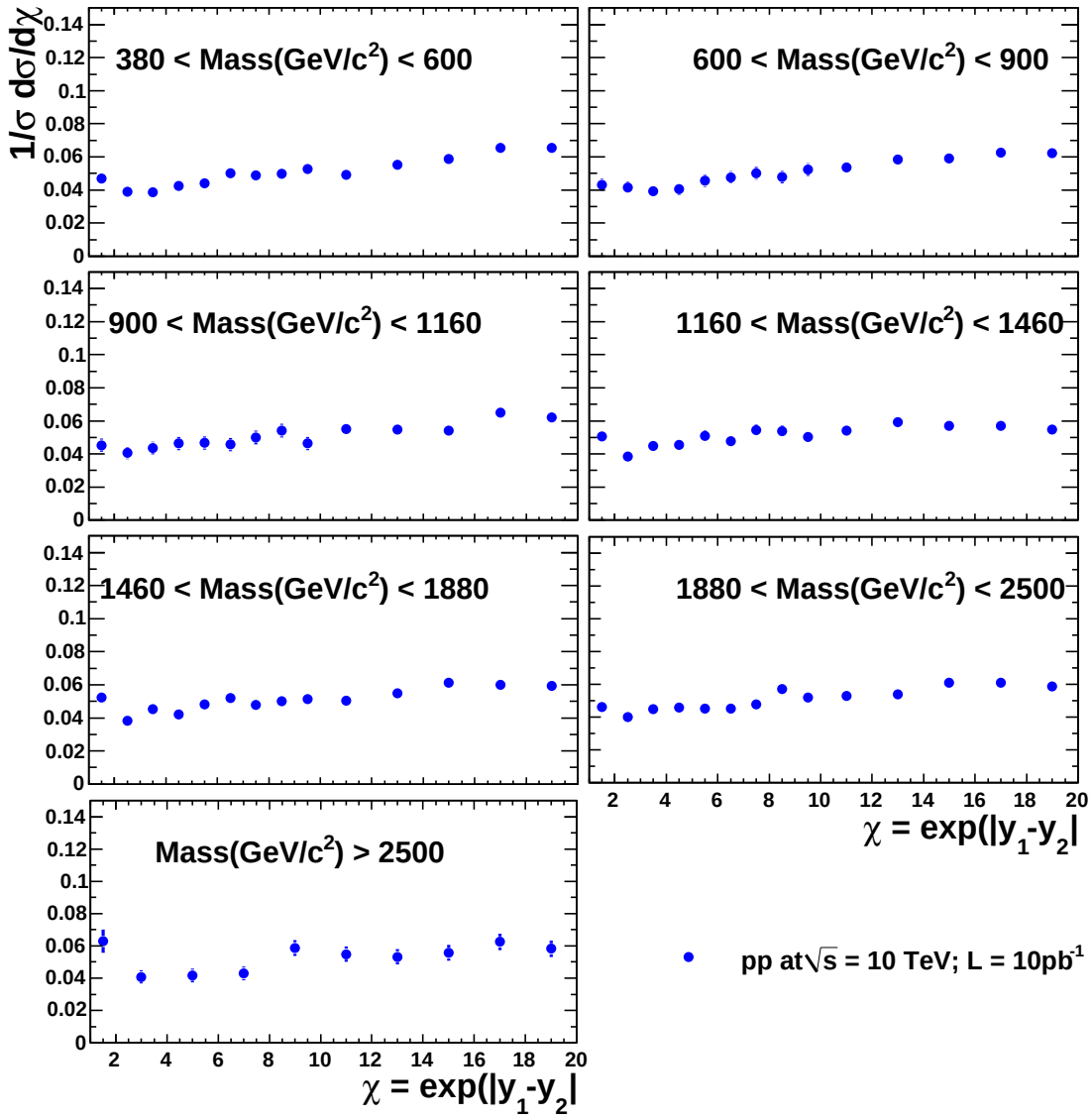

Figure 32: Dijet angular distibutions for pp collisions at $\sqrt{s} = 10\,\text{TeV}$. The statistical errors correspond to an integrated luminosity of $10\,\text{pb}^{-1}$.

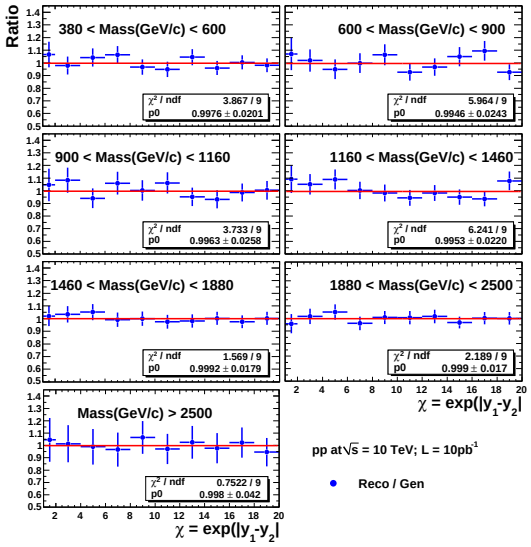

Figure 33: Relative systematic uncertainty for the χ distribution due to the jet energy scale.

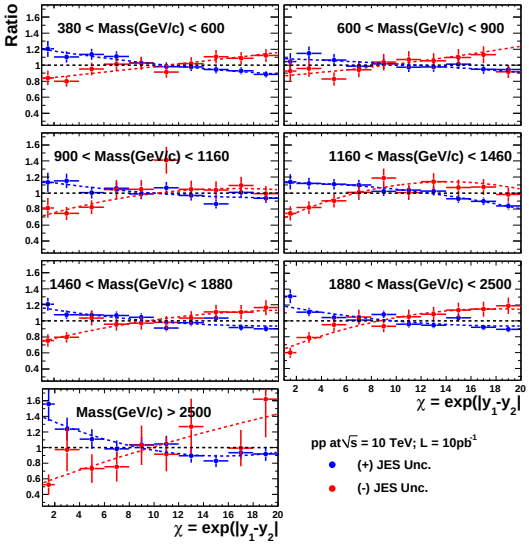

Figure 34: Systematic uncertainty due to the jet energy scale.

leading jets, is accompanied by parton radiation. In the case of soft radiation, the additional jets in the event carry small p_T and $\Delta\phi \sim \pi$, while in the case of harder radiation $\Delta\phi < \pi$. The measurement of the correlation angle $\Delta\phi$ between the leading jets, which is a simple variable, has the advantage of being insensitive to the reconstruction of low p_T radiation jets. The basic observable for this study is the differential cross section as a function of the correlation angle, divided by the integrated cross section.

$$\frac{1}{\sigma_{dijet}} \frac{d\sigma_{dijet}}{d\Delta\phi} \tag{35}$$

The choice of the particular observable ensures that the influence of theoretical and experimental uncertainties is minimal, thus allowing for early measurement.

5.1 Event Selection

The analysis presented here is restricted to the central rapidity region and thus to the barrel calorimeters of CMS. Analytically the imposed event and phase space selection criteria are the following:

- at least 2 reconstructed jets,
- $|y_1|, |y_2| < 1.1$,
- the leading jet p_T (after JES corrections) must by above the threshold where the sample becomes fully efficient.

Note that both the integrated and differential cross section appearing in equation 35 refer to the same event selection criteria.

5.2 Results

The measurement of the angular decorrelation distributions is performed in bins of the leading jet p_T. The bins are chosen such that only one fully efficient sample contributes to each bin. The bins are listed in Table (4).

The dijet azimuthal decorrelations (Figures 36,37) are strongly peaked at π, getting narrower for higher p_T bins. Overall, there are no big differences among different p_T bins.

The difference between calorimeter and generated jets distributions is presented in Figure 38. The calorimeter jets behave like particle jets for $\Delta\phi > 2\pi/3$. Below this value the difference is smaller for higher p_T bins.

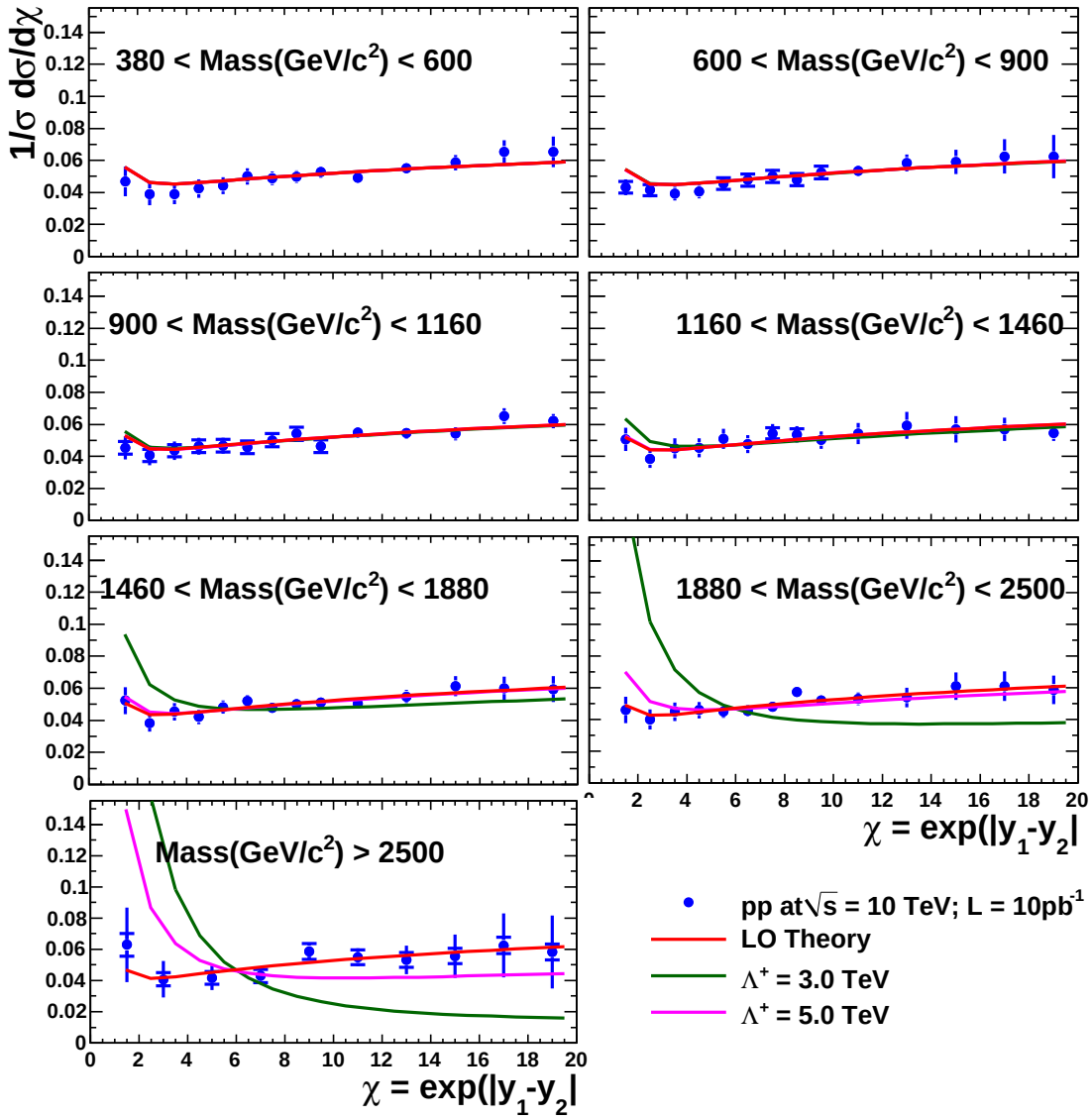

Figure 35: Dijet angular distibutions compared to LO pQCD, and to contact interactions with scales $\Lambda^+ = 3$ and 5 TeV for an integrated luminosity of $10\,\mathrm{pb}^{-1}$. The error bars represent statistical and systematic uncertainties combined in quadrature; the innermost interval indictates the statistical uncertainty.

Bin	Sample
$80 < p_T^{max} < 120$ GeV	JetET20
$120 < p_T^{max} < 190$ GeV	JetET30
$190 < p_T^{max} < 250$ GeV	JetET50
$250 < p_T^{max} < 310$ GeV	JetET80
$310 < p_T^{max} < 400$ GeV	JetET110
$p_T^{max} > 400$ GeV	JetET150

Table 7: Bins of leading jet p_T used for the azimuthal decorrelation measurement. The right column indicates the sample contributing to each bin.

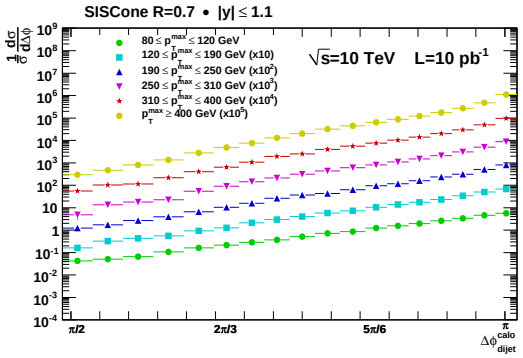

Figure 36: Measured calorimeter level $\Delta\phi$ distribution.

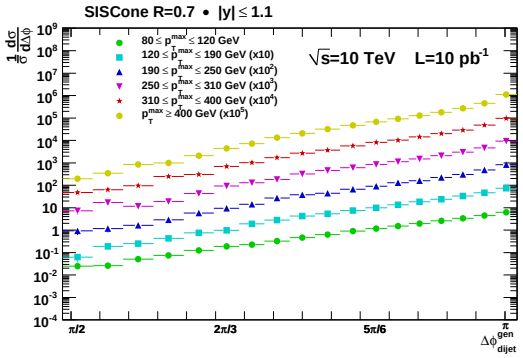

Figure 37: Measured particle level $\Delta\phi$ distribution.

5.3 Systematic Uncertainties

To investigate the discrepancy between particle and calorimeter jets at low ϕ, two further studies are presented. First, the particle jet p_T is smeared according to the energy resolution found for calorimeter jets (Section 1.5). The resulting azimuthal decorrelation distribution (Figure 39) reveals little dependence on the jet energy resolution. Second, the particle jets are smeared with the ϕ-resolution of calorimeter jets [23]. The resulting comparison (Figure 40) has similar features like the comparison to calorimeter jets and the effect is therefore attributed to the jet position resolution.

The effect of jet energy scale uncertainty on $\Delta\phi$ decorrelation is studied by considering a 10% jet energy scale uncertainty, constant in p_T and η. The effect of increasing the jet energy by 10% is shown in Figure 41, and the case of a jet energy decrease by 10% in Figure 42.

6 Conclusions

The study of high p_T jets is important for understanding QCD in the TeV scale. Also it is sensitive to phenomena beyond the Standard Model. In this note, four key analyses planned for the startup of LHC, at 10 TeV pp collisions have been presented. They have been performed using the MC samples generated for the CSA08 challenge and

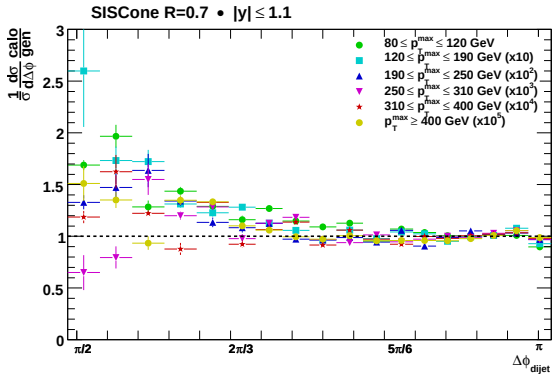

Figure 38: Ratio between calorimeter and generated distributions.

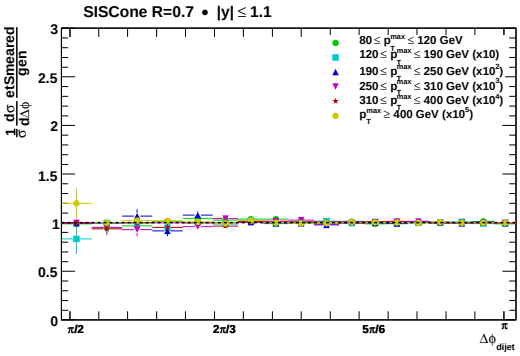

Figure 39: Jet energy smearing effect on $\Delta\phi$ decorrelation.

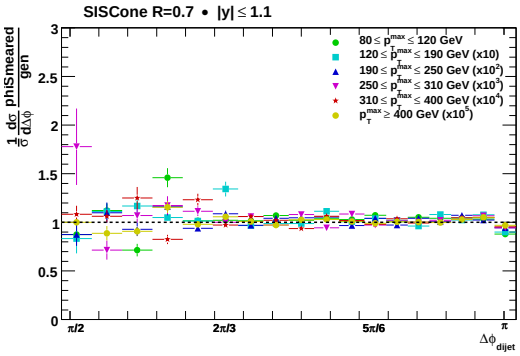

Figure 40: Jet ϕ position smearing effect on $\Delta\phi$ decorrelation.

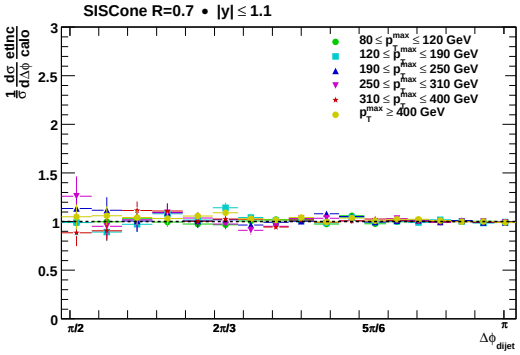

Figure 41: Jet energy scale uncertainty effect on $\Delta\phi$ decorrelation (+10%).

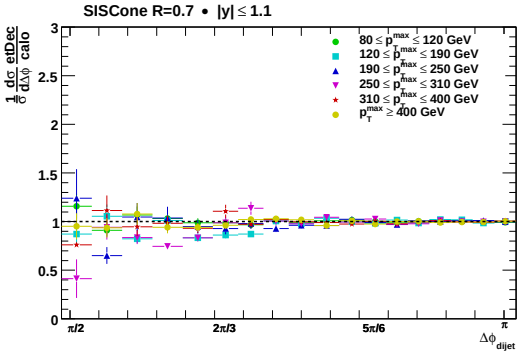

Figure 42: Jet energy scale uncertainty effect on $\Delta\phi$ decorrelation (-10%).

assuming 10 pb^{-1} of integrated luminosity. For each of these analysis topics, the steps towards the final result have been described in detail. Also the dominant systematic uncertainties have been identified and techniques for their estimation from actual data have been described.

The measurement of the inclusive jet cross section vs $\mathrm{p_T}$ is sensitive to the jet energy scale uncertainty and it is not expected to be precise enough for testing the pQCD with 10 pb^{-1}. However, the much greater $\mathrm{p_T}$ reach with respect to the Tevatron experiments and the sensitivity to new physics make this a key measurement even at startup. Similar arguments hold for the dijet cross section vs the dijet invariant mass.

The measurements of the dijet angular distributions and the dijet angular decorrelation are essentially shape analyses and as such they are almost insensitive to many experimental and theoretical uncertainties (e.g jet energy scale, luminosity). Therefore these studies can test immediately the pQCD in the TeV scale and check for phenomena beyond the Standard Model.

References

[1] S. Agostinelli et al. (GEANT4 collaboration), *"A Simulation toolkit."* **Nucl.Instr.Meth.A506:250-303, 2003**.

[2] S. Catani, Y. L. Dokshitzer, M. H. Seymour and B. R. Webber, *"Longitudinally invariant Kt clustering algorithms for hadron hadron collisions."* **Nucl.Phys.B406:187-224 (1993)**.

[3] M. Cacciari and G. P. Salam, *"Dispelling the N^3 myth for the Kt jet-finder."* **Phys.Lett.B641 57-61 (2006)**.

[4] G. P. Salam and G. Soyez, *"A practical seedless infrared-safe cone jet algorithm."* **JHEP05(2007)086 (2007)**.

[5] A. Bhatti et al., *"Plans for Jet Energy Corrections at CMS."* **CMS AN-2007/055**.

[6] Z. Nagy, *"Three-jet cross sections in hadron hadron collisions at next-to-leading order"*, **Phys.Rev.Lett.88:122003 (2002)"**, hep-ph/0110315.

[7] T. Kluge, K. Rabbertz and M. Wobisch, *"Fast pQCD calculations for PDF fits"*, hep-ph/0609285.

[8] T. Sjostrand, S. Mrenna and P. Skands, *"PYTHIA 6.4 physics and manual"*, **JHEP 0605 (2006) 026**, hep-ph/0603175.

[9] D. Acosta *et al.*, *"The underlying event at the LHC"*, **CMS NOTE-2006/067**.

[10] J. Pumplin, D. R. Stump, J. Huston, H. L. Lai, P. Nadolsky and W. K. Tung, *"New generation of parton distributions with uncertainties from global QCD analysis"*, **JHEP 0207 (2002) 012**, hep-ph/0201195.

[11] W. K. Tung, H. L. Lai, A. Belyaev, J. Pumplin, D. Stump and C. P. Yuan, *"Heavy quark mass effects in deep inelastic scattering and global QCD analysis"*, **JHEP 0702 (2007) 053**, hep-ph/0611254.

[12] S. Frixione and B. R. Webber, *"Matching NLO QCD computations and parton shower simulations"*, **JHEP 0206 (2002) 029**, hep-ph/0204244.

[13] S. Frixione and B. R. Webber, *"The MC@NLO 3.3 event generator"*, hep-ph/0612272.

[14] G. Marchesini, B. R. Webber, G. Abbiendi, I. G. Knowles, M. H. Seymour and L. Stanco, *"HERWIG: A Monte Carlo event generator for simulating hadron emission reactions with interfering gluons. Version 5.1 - April 1991"*, **Comput. Phys. Commun. 67 (1992) 465**.

[15] G. Corcella *et al.*, *"HERWIG 6.5 release note"*, hep-ph/0210213.

[16] J. M. Butterworth, J. R. Forshaw and M. H. Seymour, *"Multiparton interactions in photoproduction at HERA"*, **Z. Phys. C 72 (1996) 637**, hep-ph/9601371.

[17] M. Bahr *et al.*, *"Herwig++ 2.2 Release Note"*, arXiv:0804.3053 [hep-ph].

[18] M. Bahr *et al.*, *"Herwig++ Physics and Manual"*, arXiv:0803.0883 [hep-ph].

[19] M. Bahr, S. Gieseke and M. H. Seymour, *"Simulation of multiple partonic interactions in Herwig++"*, **JHEP 0807 (2008) 076**, arXiv:0803.3633 [hep-ph].

[20] R. Harris, K. Kousouris, *"MC Truth L2 & L3 Factorized Jet Corrections at CMS"* **CMS AN-2008/003**

[21] B. Bollen et al., *"CMS Search Plans and Sensitivity to New Physics using Dijets."* **CMS NOTE-2008/019**.

[22] B. Bollen et al., *"CMS Search Plans and Sensitivity to New Physics using Dijets."* **CMS AN-2007/039**.

[23] L. Apanasevich et al., *"Performance of Jet Algorithms in CMS."* **CMS AN-2008/001**.

[24] T. Aaltonen et al.(CDF collaboration),*" Measurement of the Inclusive Jet Cross Section at the Fermilab Tevatron p anti-p Collider Using a Cone-Based Jet Algorithm."* **arXiv:0807.2204, Submitted to Phys.Rev.D**

[25] A. Abulencia et al.(CDF collaboration),*"Measurement of the Inclusive Jet Cross Section using the k(T) algorithm in p anti-p collisions at s**(1/2)=1.96-TeV with the CDF II Detector."* **Phys.Rev.D75:092006,2007**

[26] A. Abulencia et al.(CDF collaboration),*"Measurement of the inclusive jet cross section in p anti-p collisions at s**(1/2)=1.96-TeV using a cone-based algorithm."* **Phys.Rev.D74:071103,2006**

[27] V.M. Abazov et al.(D0 collaboration),*"The Inclusive jet cross-section in p anti-p collisions at s**(1/2) = 1.8-TeV using the k-perpendicular algorithm."* **Phys.Lett.B525:211-218,2002**

[28] A.A. Affolder et al.(CDF collaboration),*"A Measurement of the differential dijet mass cross-section in p anti-p collisions at S**(1/2) = 1.8-TeV."* **Phys.Rev.D61:091101,2000**

[29] B. Abbott et al.(D0 collaboration),*"The Dijet mass spectrum and a search for quark compositeness in anti-p p collisions at S**(1/2) = 1.8-TeV."* **Phys.Rev.Lett.82:2457-2462,1999**

[30] V.M. Abazov et al.(D0 collaboration),*"Measurement of Dijet Azimuthal Decorrelations at Central Rapidities in $p\overline{p}$ Collisions at $\sqrt{s} = 1.96$ TeV."* **Phys.Rev.Lett.94:221801,2005**

[31] V.M. Abazov et al.(D0 collaboration),*"Measurement of the inclusive jet cross-section in p anti-p collisions at s**(1/2) =1.96-TeV."* **arXiv:0802.2400, Submitted to Phys.Rev.Lett.**

[32] B. Abbott et al.(D0 collaboration),*"High-pT jets in p? p collisions at sqrt[s]=630 and 1800 GeV."* **Phys.Rev.D64:032003,2001**

[33] E. Eichten, K. Lane, and M.E. Peskin, *"New Tests for Quark and Lepton Substructure"* **Phys.Rev.Lett.50:811-814 (1983)**

[34] K. Lane, *"Electroweak and Flavor Dynamics at Hadron Colliders"* **BUHEP-96-8 (1996)**, hep-ph/9605257.